Effect of Scouring in Sand on Monopile Supported Offshore Wind Turbines

Abhinav K A[a], Nilanjan Saha[a,*]

[a]*Dept. of Ocean Engineering, Indian Institute of Technology - Madras, Chennai, India*

Abstract

This paper analyzes the influence of scour on the overall response of monopile supported offshore wind turbines (OWTs) in 20 m water depth. Scouring effects on OWTs have been often studied within the geo-technical domain, considering static loads at the mudline. The present work attempts to address the scour induced problems in OWTs by making use of an integrated aerodynamic-hydrodynamic load approach. The OWT analysis is simulated for operational and shut-down (parked) condition. Under parked situations, the OWT blades are feathered and power production is suspended, owing to structural safety concerns. 50 Monte Carlo responses of stochastic sea state condition (wind speed with turbulence, significant wave height and peak spectral period) are generated. Irregular, long-crested waves are generated using the Joint North Sea Wave Project (JONSWAP) spectrum. Then from each simulation, the ensemble response is obtained. Sandy soil of varying densities are considered. Results indicate that OWTs founded on loose sands suffer significant stiffness (and hence natural frequency) reductions, shifting the structure into the resonance regime. Lateral responses also show an escalation with reduction in density of sandy soil.

Keywords: Monopile, Offshore wind turbines, Scouring, Random response analysis

2010 MSC: 00-01, 99-00

*Corresponding author

Email address: nilanjan@iitm.ac.in (Nilanjan Saha)

1. Introduction

Power from offshore wind is expected to play a significant role in offsetting the impending non-renewable energy crisis. Offshore wind turbines (OWTs) are supported on monopiles in shallow waters. The presence of an offshore structure such as a pile, gives rise to local currents and waves. These variations in local flow phenomena causes the motion of cohesion-less soil particles away from the structure, resulting in scouring [1]. This removal of soil from the top layers (both local and global) results in significant reduction of lateral support for the OWT, leading to excessive displacements and rotations. A comprehensive description of the mechanism of scouring and its influence on offshore structures can be found in [2]. The influence of scouring on the natural frequency of an OWT has been investigated by [1], [3] and [4]. [5] attempted to quantify the influence of scour on laterally loaded monopiles, under static and cyclic loading, but only the sub-soil domain was considered.

Studies on the soil-structure interaction (SSI) of OWTs under scouring are mostly limited to static analyses. According to [6], dynamic behaviour becomes significant for structures with natural periods greater than 3 s. Even in dynamic framework, the combination of aerodynamics, hydrodynamics and geotechnical effects have not been considered [7, 8, 9]. Moreover, as an OWT is influenced by irregular dynamic loading from wind and waves, there arises also a need to investigate its response within a stochastic time-domain framework.

This paper attempts to characterize the degree of influence of scour on the stochastic lateral response of OWTs in sand in Indian offshore. The response of OWT is simulated in a Lagrangian based finite element (FE) method. The time domain simulation is performed for 600 s under combined wind and wave loads. In accordance with [10] the scour development around the monopile is assumed to be local. Further, the maximum scour depth is considered as 1.5 times the pile diameter [11].

Note that the stationary condition with respect to wind speed is 10 min

whereas it is 3 hr for the waves. So if one uses 3 hr for simulation of OWT, 18 sets of varying wind speed will be necessary which would introduce aleatory (natural uncertainty) and epistemic (knowledge based) uncertainties. One cannot avert the aleatory uncertainty arising from irregularity of the wind and waves, however one should be able to prevent the errors proliferating from the data and statistical uncertainty if one uses 10 min condition for generation of wind speeds. Initially, the geotechnical and the natural frequencies of the model are validated with similar studies. The investigation on the influence of scour depth on the natural frequency shows that for loose sands, one has to periodically monitor such that resonance condition is avoided in scour prone areas. The results are presented for ensemble mean of realizations of the lateral response of a monopile supported OWT in varying stiffness (loose, medium-dense and dense sands).

2. Description of the Numerical Model

2.1. OWT model

A numerical model of a monopile supporting the NREL 5 MW OWT [12] in a water depth of 20 m is developed using the FE program USFOS [13]. The monopile has an outer diameter of 6 m and a penetration depth of 36 m below the mudline. The properties of the OWT model are listed in Table 1. Two-noded beam-column elements are used for the monopile and the soil-structure interaction (SSI) is modelled by means of discrete soil springs along the pile. Lateral (p-y), axial (t-z) and end bearing (Q-z) soil spring parameters are derived on the basis of [11] and [10] recommendations. Scour is accounted for, by removing the relevant springs from the numerical model. The concept of a monopile supported OWT is shown in Figure 1.

2.2. Validation

The capability of USFOS to model lateral response of piles is validated by comparison with the p-y method demonstrated in [14]. As shown in Figure 2,

Table 1: Properties of NREL 5 MW OWT [12]

Parameter	Value
Power rating	5 MW
Rotor orientation	Upwind
Rotor, Hub diameter	126 m, 3 m
Rated rotor speed	12.1 rpm
Cut-in wind speed	3 m/s
Rated wind speed	11.4 m/s
Cut-out wind speed	25 m/s
Rotor-nacelle-assembly mass	$350,000$kg
Tower base diameter, thickness	6 m, 27 mm
Tower top diameter, thickness	3.87 m, 19 mm
Elevation of tower top	87.6 m above MSL

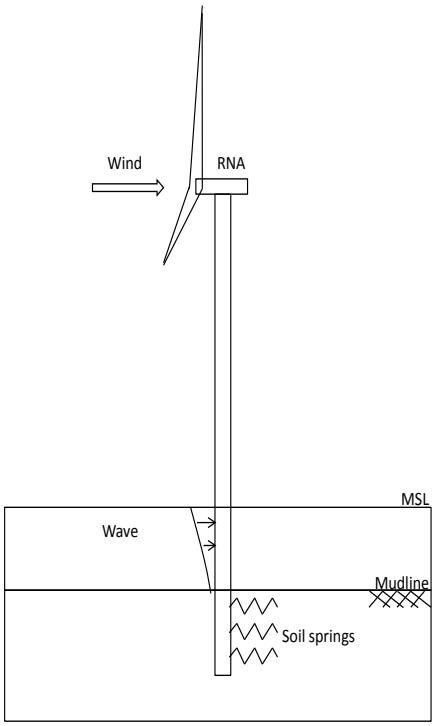

Figure 1: Monopile supported OWT

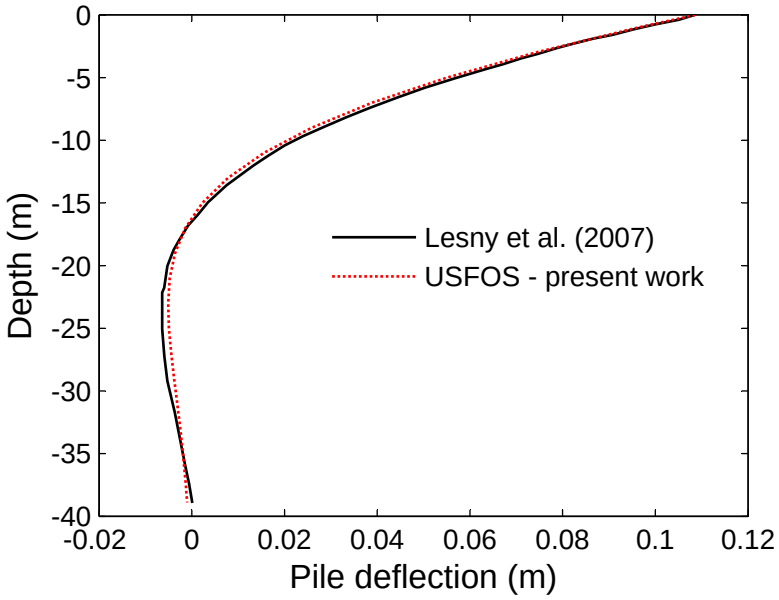

Figure 2: Validation of the numerical model - pile displacement analysis

the prediction by USFOS, for a pile of 6 m diameter and 39 m penetration in dense sand and subjected to a mudline moment of 855 MN-m, closely matched the reported curve, thereby confirming its suitability to handle the monopile problem.

A second validation test was performed with respect to natural frequency of a bottom fixed monopile OWT, for the Opti - OWECS model. The fundamental natural frequency obtained using USFOS is reasonably close to the ones predicted by the analytical equation (1) of [15], as shown in Table 2. The test has been repeated for various monopile diameters.

$$f_1 = \frac{D}{L^2}\sqrt{\frac{E}{104(a+0.227)\rho_c}} \tag{1}$$
$$a = \frac{M}{\rho_c \pi D t L}$$

Here, f_1 is the fundamental natural frequency of the bottom fixed monopile OWT, while D and L stands for the diameter and length of the tower, respec-

tively. E and ρ_c refer to the modulus of elasticity and density of the material (steel), respectively. M is the mass of the turbine located at the top of the tower and t is the thickness of the wall of the tower.

Table 2: Validation of the numerical model - natural frequency analysis

Diameter	[15]	USFOS
2.4 m	0.25 Hz	0.22 Hz
4.2 m	0.50 Hz	0.47 Hz
7.4 m	1.00 Hz	0.94 Hz

3. Methodology of Analysis

An integrated OWT analysis encompasses aerodynamic, hydrodynamic and geotechnical domain. The following subsections describe in detail, the generation of wind and wave loads for dynamic analysis.

3.1. Aerodynamic Loads

Spatial and temporal variations are characteristics of stochastic winds. Wind speed simulation should account for these variations. The following subsections address the modelling theory for stochastic wind.

3.1.1. Wind velocity vertical profile

Wind speed is influenced by the frictional interaction with the earth's surface. As a result, inside the atmospheric boundary layer, the mean wind speed increases steadily with height - this phenomenon is called wind shear. As the output of a wind turbine is proportional to the cube of the mean wind velocity, it becomes important to study the wind shear [16]. The variation of wind velocity with height above the earth's surface, is usually determined by means of the logarithmic law or the power law.

$$V(z)/V(z_r) = ln(\frac{z}{z_0})/ln(\frac{z_r}{z_0}) \tag{2}$$

The power law profile is given by:

$$V(z)/V(z_r) = (\frac{z}{z_r})^{\alpha} \tag{3}$$

Here, $V(z)$ and $V(z_r)$ are the mean wind speed at the an elevation of z, and the mean wind speed at a reference height, z_r respectively, z_0 is the roughness parameter and α is the power law coefficient.

For offshore conditions, [17] suggests values of 0.0001 - 0.003 for z_0 and 0.12 for α, respectively. The variation in wind speeds computed using the logarithmic and power laws are small ($< 1\%$) [18]. The winds encountered by OWTs are often turbulent in nature. It refers to the random, short-term variations that the mean wind speed is subjected to, during the conversion of the kinetic energy in the wind, to thermal energy [16]. Turbulence is usually defined in terms of the turbulence intensity (TI), *i.e.* ratio of the standard deviation of the wind speed to its mean.

Figure 3 compares the wind shear profiles using both logarithmic and power laws. A mean wind speed of 11.4 m/s (*i.e.*, the rated wind speed of the NREL 5MW OWT) is used, with a turbulence intensity of 11%. For the example given in Figure 3, $z_0 = 0.001$ and $\alpha = 0.12$ are used by logarithmic law and power law, respectively. Usually, wind shear profiles are computed about the hub height and the differences between the two laws even out, over the rotor diameter [19]. The present study uses the logarithmic profile to account for wind shear.

3.1.2. Generation of 3D wind

3-dimensional full field stochastic wind fields are generated by means of NREL's simulator, TurbSim [20]. The SANDIA method [21] is made use of, for realizing 3-dimensional turbulent wind fields. Initially, a suitable frequency domain description of the wind velocity is assumed. The present work makes use of the Kaimal spectrum [22], described by equation 4.

$$S_{Kaimal}(f) = \frac{4{\sigma_v}^2 L_k/v_h}{(1 + 6fL_k/v_h)^{5/3}} \tag{4}$$

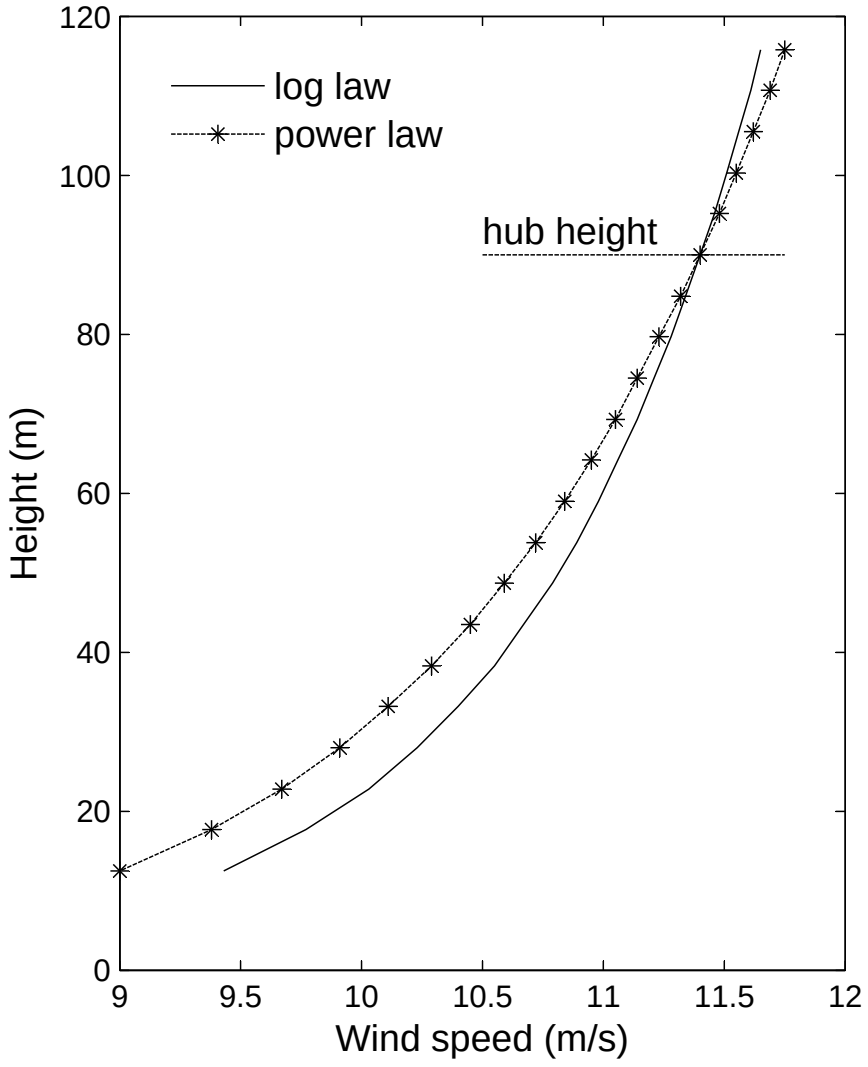

Figure 3: Comparison of wind speeds from log and power laws

where f is the cyclic frequency, L_k is an integral length scale parameter, v_h is the mean wind speed and σ_v is its standard deviation. By means of FFT, time histories of wind speed vectors are now generated at several points in a rectangular plane, which encloses the turbine rotor. The grids containing the time series are now marched in the mean wind direction, at the mean wind

speed, making use of Taylor's frozen turbulence hypothesis. This concept is illustrated in Figure 4. A grid size of 155 m × 155 m is chosen, so that the turbine rotor is fully encompassed by the wind field. Size of the time step is 0.05 s.

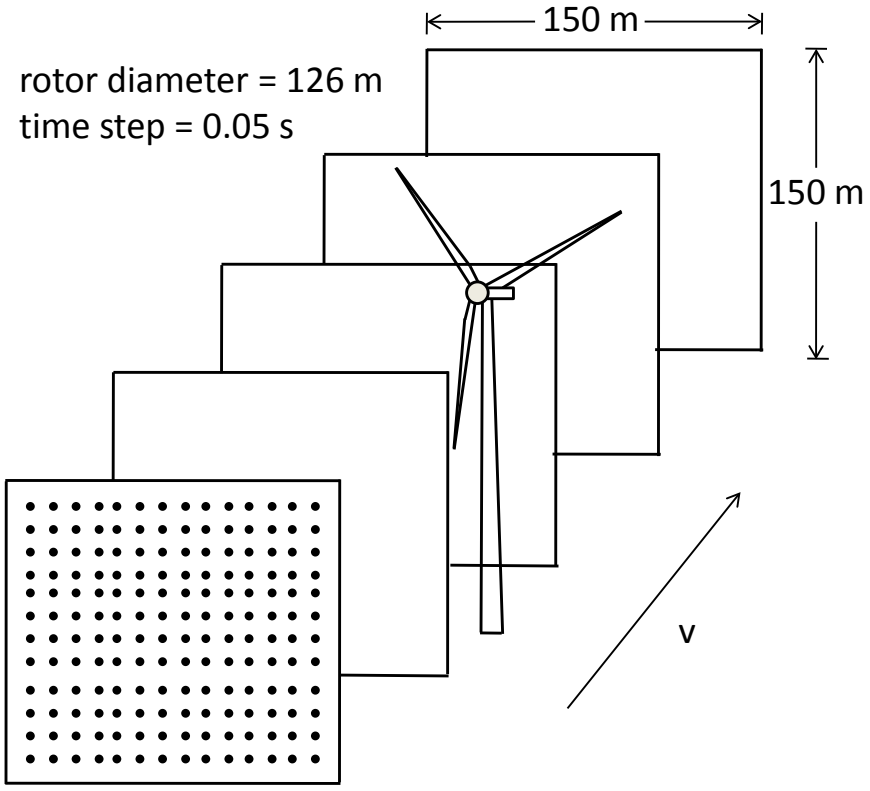

Figure 4: Grids of wind velocity vectors marching past the rotor

Figure 5 shows a sample wind velocity time histories for turbulent and uniform winds of 11.4 m/s, at the hub height of the OWT. The turbulent wind has a corresponding turbulence intensity of 11%. The effect of turbulence on the mean wind speed is clearly discernible.

3.1.3. Computing aerodynamic loads

The time series of load components acting on the hub of the OWT are derived using NREL's code, FAST [23]. Through linear interpolation of the

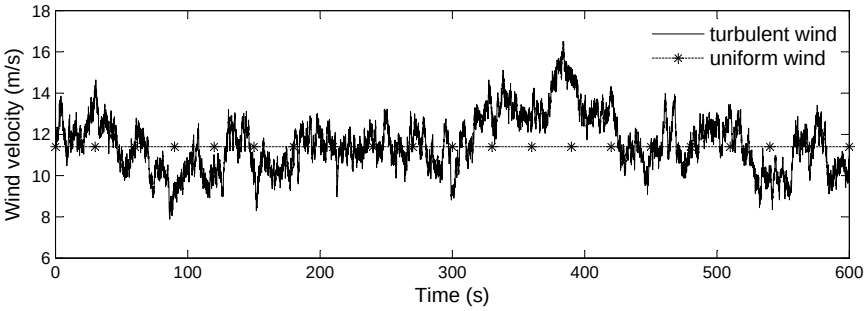

Figure 5: Time history of wind velocity

3-dimensional wind data, FAST computes the wind velocity components at the blade element locations. The aerodynamic loads on the hub and the blades of the turbine are now calculated using the Blade Element Momentum (BEM) theory [24]. The BEM theory, popular owing to low computational costs, is founded on the following assumptions - stiff blades, no aerodynamic interaction among individual blade components, absence of radial flow and forces depend only on the lift and drag properties of the airfoil.

The BEM theory has two parts - the blade element theory and the momentum theory. According to the former, a blade is discretized into radial elements as shown in Figure 6 and the total aerodynamic force acting on it can be obtained by summing up the loads on the individual components. The latter theory states that the momentum loss at any radial section is due the action of the local axial forces produced by the airflow, on the blade elements [25]. Combining these two theories gives an iterative (BEM) procedure to compute the aerodynamic forces.

Aerodynamic forces are composed of lift and drag. Horizontal axis wind turbines, such as the one considered in the present study, makes use of the lift force, which is perpendicular to the relative flow direction, for their operation. Drag forces act parallel to the flow. These force components are depicted in Figure 7.

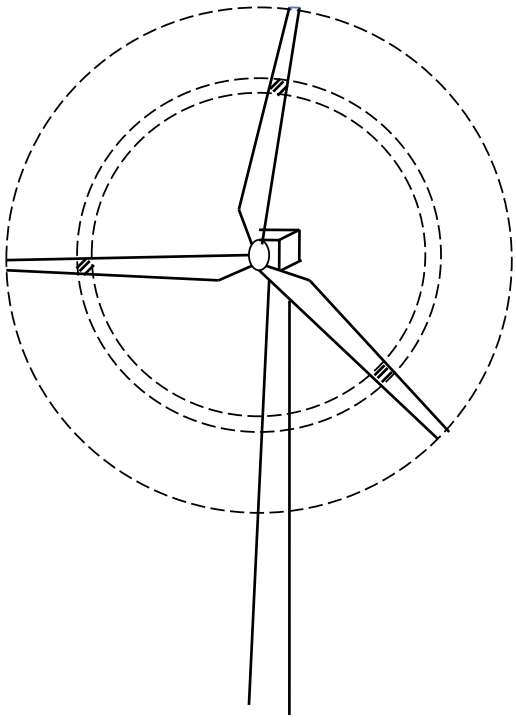

Figure 6: Annular rings traced by the rotor

The lift and drag forces per unit length can be written as:

$$f_L = \frac{\rho c}{2} V_{rel}^2 C_L(\alpha) \tag{5}$$

$$f_D = \frac{\rho c}{2} V_{rel}^2 C_D(\alpha) \tag{6}$$

Here, C_L and C_D are lift and drag coefficients, obtained as functions of the angle of incidence, α and c is the chord length of a blade element. The local flow direction makes an angle of ϕ with the rotor plane and β is called the pitch angle.

3.2. Hydrodynamic Loads

The uncertain sea environment can be best described by means of irregular waves. The generation of wave time series and computation of wave forces on

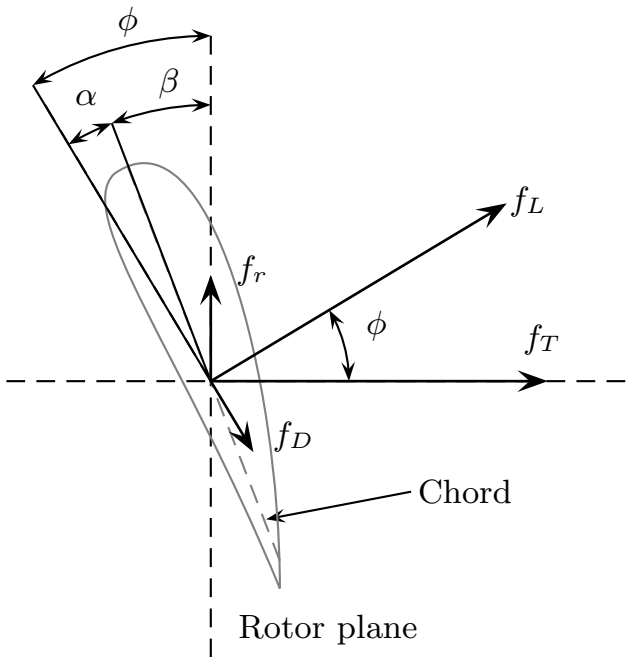

Figure 7: Forces on a blade element [26]

the OWT are described in the following subsections.

3.2.1. Generation of wave surface profile

Time series of irregular wave profiles are generated from the JONSWAP wave spectrum [27], represented by equation 7. Here, α is the Phillips constant (has a value of 0.0081), g is the acceleration due to gravity, ω_0 is the spectral peak frequency and γ is a peakedness parameter, with an average value of 3.3. The JONSWAP spectrum is valid for severe sea states and limited fetch (area of sea over which the wind blows, resulting in wave generation) and is applicable for Indian waters [28].

$$S(\omega) = \alpha g^2 \omega^{-5} exp(-1.25[\frac{\omega}{\omega_0}]^{-4}) \gamma^{exp\frac{-(\omega-\omega_0)^2}{2\sigma^2\omega_0^2}} \tag{7}$$

Irregular waves can be simulated by superposition of a number of harmonic wave components with random phase lag. Initially, the spectrum is divided

into a finite number of components using Borgman's equal area method [29], as shown in Figure 8. Here, the spectrum is divided into N equal areas (or energy). Each of these component areas can be depicted as harmonic waves with given amplitude and angular frequency. As the areas under the different components of the spectrum are equal, all corresponding regular waves have equal amplitudes, a_i, given by:

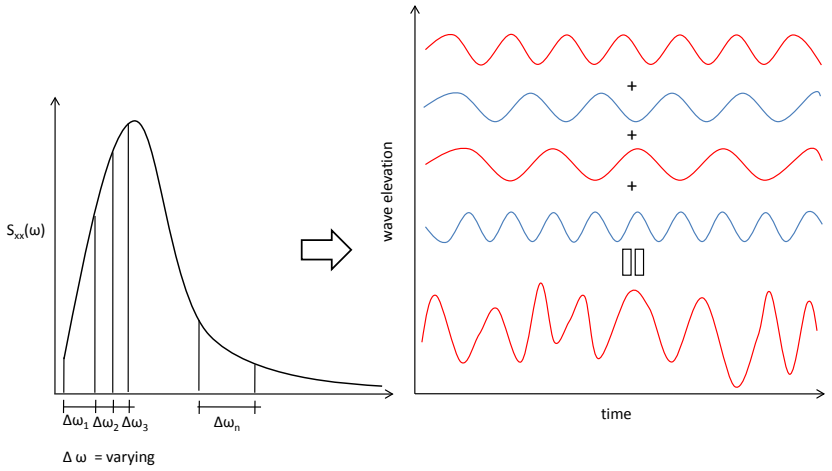

Figure 8: Constant area discretization of wave spectrum to generate irregular wave surface profile

$$a_i = \sqrt{2 \int_{\omega_{l,i}}^{\omega_{u,i}} S(\omega) d\omega} = \frac{\sqrt{2 \int_{\omega_l}^{\omega_u} S(\omega) d\omega}}{N} \tag{8}$$

Here, $\omega_{l,i}$ and $\omega_{u,i}$ are the lower and upper limits of angular frequency, for the i^{th} wave component, ω_l and ω_u are the lower and upper bounds of angular frequency of the spectrum and N is the number of components into which the spectrum is divided. The irregular wave profile is now obtained by superposing all the component harmonic waves, as given by [30, 31]:

$$\eta(t) = \sum_{i=1}^{N} a_i \cos(\omega_i t - \epsilon_i) \tag{9}$$

ϵ_i are the random phases included to maintain the randomness of the time

histories. Pseudo-random number generators are used to realize random phases over the interval $\mathcal{U}(0, 2\pi)$. Figure 9 illustrates a sample realization of the sea surface elevation, corresponding to a significant wave height H_s of 3.1 m and a peak spectral period T_p of 10.1 s.

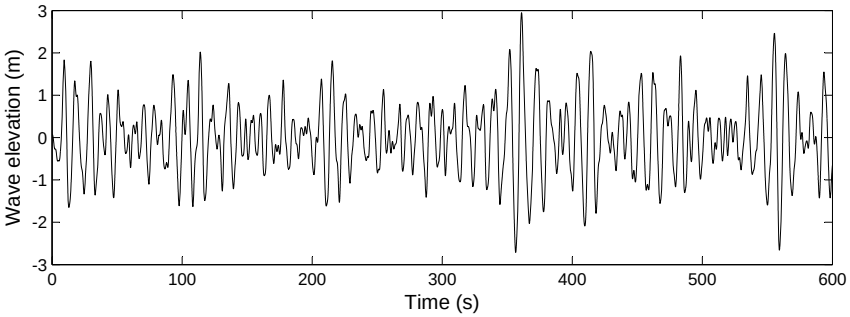

Figure 9: Sample realization of sea surface elevation

3.2.2. Wave loads on the OWT

On generating the irregular wave surface profile, the hydrodynamic loading on fixed cylinders, like a monopile can be computed using Morison's equation [32], as given in (10). A schematic representation of wave loads acting on a cylindrical pile of diameter D, is shown in Figure 10.

A linear inertia and a nonlinear drag components account for the total hydrodynamic force. The inertia force is proportional to the water particle acceleration and is exerted by the fluid, as it accelerates and then decelerates while moving past the cylinder. The drag force is attributed to the pressure difference between the upstream and downstream side of the cylinder. It is proportional to the square of the water particle velocity and the absolute value sign ensures that it acts in the same direction as the velocity.

$$f = \rho C_M \frac{\pi D^2}{4} \dot{u} + \frac{1}{2} \rho C_D |u| \; u \tag{10}$$

Here, f is the horizontal force per unit length of the pile, D is the diameter of the cylinder and u is the relative water particle velocity in the horizontal di-

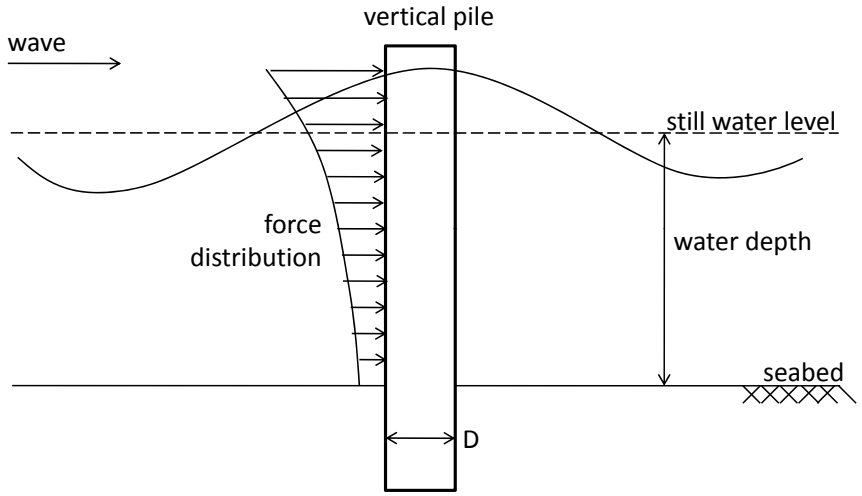

Figure 10: Wave force distribution on a vertical pile

rection. C_M and C_D are the empirical inertia and drag coefficients, respectively and ρ is the density of water. The upper dot represents the time derivative. In the present study, values of 2.0 and 0.7 are used for inertia and drag coefficients, respectively [33].

3.3. Modelling of Soil

Monopiles supporting OWTs have large diameters that vary from 4 - 7 m. p-y curves were developed for use in laterally loaded small diameter piles, that show flexible behaviour. On the other hand, under extreme loads, large diameter monopiles behave as rigid bodies, *i.e.*, they rotate about a pivot point, displaying the toe-kick phenomenon [34]. However, despite this limitation, leading offshore design standards like [11] and [10] recommend the use of p-y curves for monopiles [35].

For the present study, soil-structure-interaction is modelled using spring-to-ground elements, in line with the Winkler model. Springs representing the soil behaviour in both axial and lateral directions are attached to the pile at discrete locations along its length, and also at the tip of the pile, as shown in Figure 11. The distance between the lateral spring elements effectively define the density

of the finite element mesh for the pile element. After performing a numerical convergence study, a spacing value of 3 m is used for the present work.

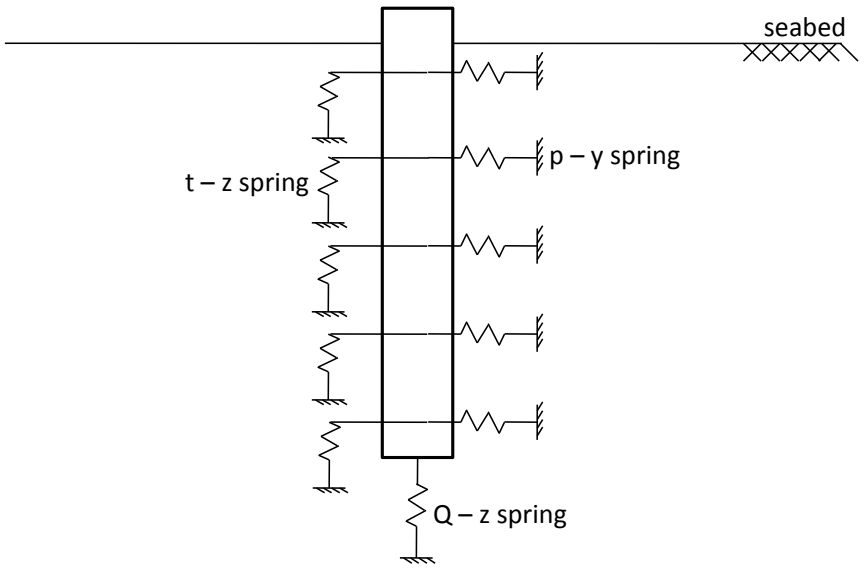

Figure 11: Representation of pile-soil model

The spring properties are defined by means of (p-y), (t-z) and (Q-z) curves recommended by offshore standards [11, 10]. The derivation of these curves are discussed in detail by authors such as [36], [33]. For the sake of brevity, only p-y curves for sand are mentioned. [11] defines p-y curves for sand as follows:

$$p = Ap_u tanh\left(\frac{kx}{Ap_u}y\right) \tag{11}$$

where the value of A depends on the nature of the loading. A_s and A_c are used for static and cyclic loading, respectively.

$$\begin{aligned} A_s &= \left(3.0 - 0.8\frac{x}{D}\right) \geq 0.9 \\ A_c &= 0.9 \end{aligned} \tag{12}$$

In the above equations, p_u is the ultimate lateral bearing capacity at a depth x and k is the initial modulus of subgrade reaction, obtained from [11], as

a function of ϕ, the angle of internal friction. p_u values are computed for both shallow and deeper depths, as p_{us} and p_{ud} respectively and the lower value is used as the ultimate lateral bearing capacity (equation 13) for sand.

$$\begin{aligned} p_{us} &= (C_1 \times x + C_2 \times D) \times \gamma \times x \\ p_{ud} &= C_3 \times D \times \gamma \times x \end{aligned} \tag{13}$$

where p_u is the ultimate lateral resistance for shallow (s) and deep (d) conditions respectively, γ is the effective unit weight of soil, D is the pile diameter and C_1, C_2 and C_3 are coefficients dependent on the angle of internal friction, ϕ, as obtained from [11].

3.4. Static Pushover Analysis

Pushover analysis gives an insight into the resistance of an offshore structure to forces arising from a single large wave [37]. Pushover analyses are done by incrementing the lateral loads (for instance, wave) acting on a structure to simulate its collapse. Nonlinear static pushover analyses supply a host of information about the structure - its initial yield, ultimate capacity, seismic response, progression of failure and residual strength. The initial relationship between load and displacement, when it behaves as elastic, is linear. However, with increase in load, the structure enters the plastic regime, accompanied by a corresponding reduction in stiffness and displacement increases without any significant increase in the load. The term yield point refers to the point of maximum curvature on the load - displacement profile [38].

USFOS runs on a modified Lagrangian formulation, wherein the system stiffness equations are solved and the structural configuration (element reference axes and forces) updated with each load step [13]. The displacement derivatives are determined on the basis of the final step of the computed configuration and not the actual configuration, unlike in a total Lagrangian formulation, where the original coordinate system is maintained.

Nonlinear analyses typically use the determinant of the stiffness matrix, to check for stability of a structure. Stable structures have positive determinants.

With increasing loads, the response of the structure shifts gradually into the nonlinear regime and the determinant deceases. A determinant value of zero indicates the presence of a bifurcation point and a further decrease makes the structure unstable. In USFOS, the structural stiffness is represented by means of a normalized current stiffness parameter (CSP). The CSP (14) can be thought of as the ratio of the incremental work done in the first load step, to the incremental work at a particular load step, i. The CSP has an initial value of 1 and it decreases with increasing load and decreasing stability [39].

$$S^i = \frac{(\Delta r^1)^T . \Delta R^1 . (\Delta p^i)^2}{(\Delta r^i)^T . \Delta R^i . (\Delta p^1)^2} \tag{14}$$

where S^i is the current stiffness parameter for the i^{th} step. ΔR and Δr stand for the incremental forces and displacements and Δp represents the size of the relative load increment at each load step.

3.5. Dynamic Analysis

The code USFOS makes use of the Hilber-Hughes-Taylor (HHT)-α method [13] for numerical time integration. The α parameter represents the time averaging of damping, stiffness and load. A relative damping of 5% for the eigen modes is considered. This method has the advantage of considering artificial damping of higher modes, while maintaining the accuracy. The accuracy and stability of the integration are represented by three parameters, α, β and γ. The HHT-α method attains unconditional stability under the following conditions:

$$\begin{aligned} -\frac{1}{3} < \alpha < 0 \\ \gamma = \frac{1}{2}(1 - 2\alpha) \\ \beta = \frac{1}{4}(1 - \alpha)^2 \end{aligned} \tag{15}$$

3.6. Combining Aerodynamic and Hydrodynamic Loads

Due to the lack of a platform capable of integrated aerodynamic-hydrodynamic-geotechnical analysis of OWTs, it is required to sequentially couple aerodynamic

codes like FAST, with a structural analysis program such as USFOS, to obtain the overall dynamic response. In the case of fixed-bottom-fixed OWTs (monopiles, in this case), such a coupled wind-wave analysis yields conservative results, when the natural period of the structure is lower than the period of the environmental forces [40, 41]. Such an analysis can be performed in two steps, as shown in Figure 12.

Initially, both aerodynamic and hydrodynamic loading are applied on the monopile model in FAST, with its base fixed at the mudline. The aerodynamic force components acting at the OWT hub are now obtained as time series of loads. In the second step, the OWT model is built in USFOS (including the soil components) and is subjected to hydrodynamic loading along with aerodynamic loading in the form of time series of hub height loads obtained from the first step, resulting in an integrated aerodynamic-hydrodynamic-geotechnical analysis.

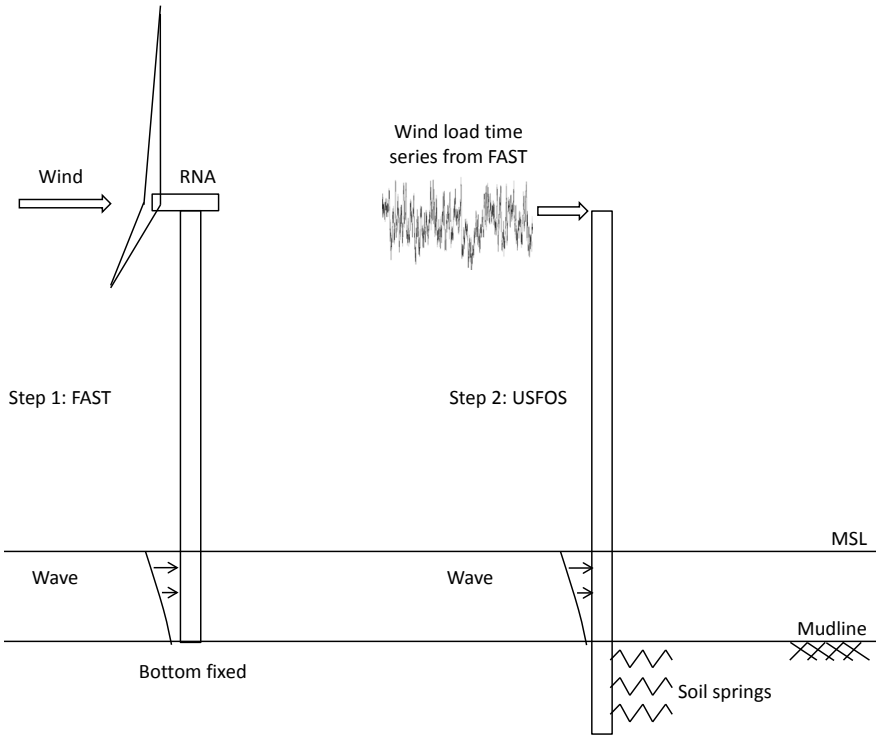

Figure 12: Coupling of load effects

3.6.1. Uncertainty analysis

As mentioned in the previous subsections, wave (and wind) time series are generated by use of random phases (or seeds). The use of random seeds ensures that the same realization of a time series can be obtained while using the same program, regardless of the computer [9]. For the same wave (or wind) conditions, the use of different random seeds would essentially generate different time histories. The use of random, single, time histories for analysis would thus result in the so-called statistical uncertainty, which is epistemic (attributed to a lack of knowledge of the process) in nature [42]. Figure 13 shows an example of statistical uncertainty, with respect to the kurtosis of tower top displacement.

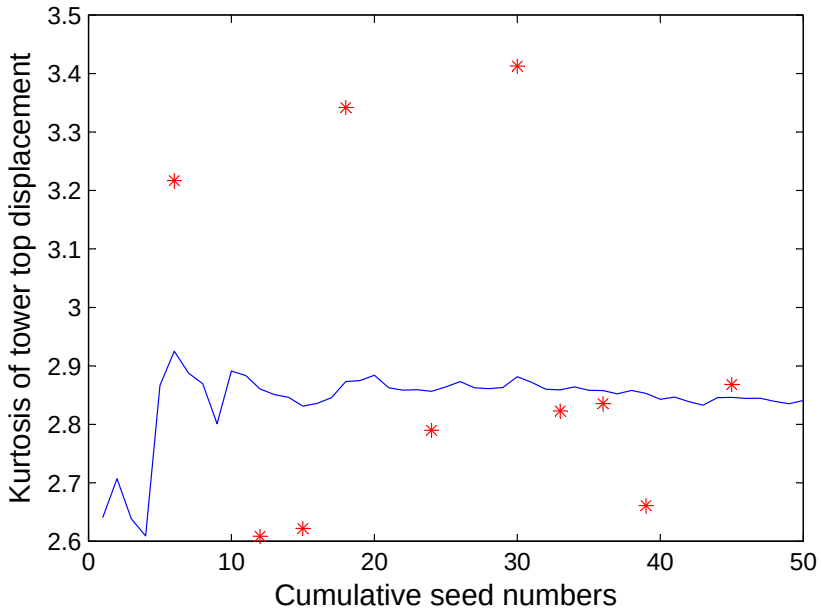

Figure 13: Eliminating uncertainty effects

The red points in Figure 13 indicate the value of kurtosis for 10 individual random seeds. The variations in the estimated property (kurtosis, in this case), while using single time histories for dynamic analyses can be understood from the figure. This uncertainty due to time domain simulation can be eliminated

by increasing the number of simulations, using different time series of wind and wave, generated using varying random seeds and obtaining the mean values of the relevant statistical parameters. The blue continuous line in Figure 13 shows the convergence of the kurtosis values, with increase in the number of simulations. Convergence is noted to be attained with $20 - 25$ random seeds. However, in the present work, 50 Monte Carlo simulations are used to generate each realization of the irregular sea surface and wind speed (and thus, the loading).

3.7. Modelling Parameters

Uniform sandy soil profiles of varying density, as shown in Table 3, are used for the study. These types of weathered sandy soils are situated in eastern Indian offshore. Here, γ', Φ and K stands for the effective unit weight of soil, the angle of internal friction and the modulus of subgrade reaction, respectively.

Table 3: Classification of sands used in the study based on [43]

Density	γ' (kN/m^3)	Φ ($^\circ$)	K (MN/m^3)
loose	10	29	2.6
medium dense	10	35	24.4
dense	10	39	38.0

Two different load cases (LC's) are considered for dynamic analysis, as detailed in Table 4. LC1 relates to an operational condition, where a mean hub-height (HH) wind velocity (V) of 11.4 m/s, *i.e.* the rated value for the NREL 5 MW OWT is considered. At the rated wind speed, the OWT achieves its maximum power output. LC2 pertains to an extreme situation where the mean HH wind speed of 27 m/s is greater than the cut-out wind speed for the NREL 5 MW OWT (25 m/s). JONSWAP spectrum is recommended for use in the Indian coastal waters, by [28]. The corresponding sea-states, correlated on the wind speed, are defined by expected values of a significant wave height (H_s) – spectral peak period (T_p) pair on the basis of [44].

Here, the significant wave height is represented by a Weibull distribution [45] and its expected value is given by:

$$E(H_s) = \beta\Gamma(\frac{1}{\alpha} + 1) \tag{16}$$

For the North Sea, [44] has defined the shape and scale parameters as $\alpha = 2 + 0.135v$ and $\beta = 1.8 + 0.1v^{1.322}$, respectively, where v is the wind speed. The peak period is described by a lognormal distribution, conditional on the wind speed and significant wave height [44] and its expected value is obtained as:

$$\begin{aligned} E(T_p) &= (4.883 + 2.68H_s^{0.529}) \\ &\times \left\{1 - 0.19(\frac{v - (1.764 + 3.426H_s^{0.78})}{1.764 + 3.426H_s^{0.78}})\right\} \end{aligned} \tag{17}$$

A scour parameter is defined as the ratio of the scour depth (s) to the monopile diameter (D). s/D value of 0 implies the no scour condition and a maximum value of 1.5 is considered, as per [11] recommendations. Dynamic analyses are of 600 s in duration. 50 stochastic simulations (using varying wind and wave fields for the same wind speed - sea state combination) are performed for each case, to eliminate the uncertainty arising from time-series generation, and the ensemble mean values are reported.

Table 4: Load case parameters

Load case	V (m/s)	H_s (m)	T_p (s)	Remarks
LC1	11.4	3.1	10.1	Operating
LC2	27.0	6.4	11.5	Parked

4. Results

4.1. Natural Frequency Analysis

Natural frequency is a design driver for OWTs. They are susceptible to low frequency excitations from wind and wave loading. Other sources of excitations are the rotor (1P) and the blade-pass (3P for a 3-bladed turbine) frequencies.

For the NREL 5 MW OWT, 1P and 3P frequencies lie in the ranges $0.115-0.2$ Hz and $0.345-0.6$ Hz respectively [46]. To avoid resonance, OWTs are designed to have their natural frequencies in the safe zone between 1P and 3P values. This philosophy is called the soft-stiff design.

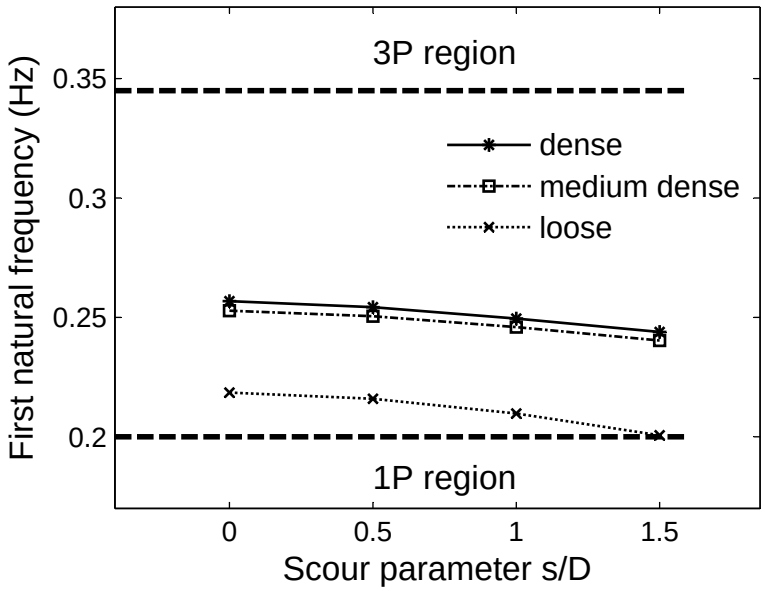

Figure 14: Variation of first natural frequency with scour depth

Table 5: First and second natural frequencies of the OWT

s/D →	0	0.5	1.0	1.5
First natural frequency (Hz)				
loose	0.219	0.216	0.210	0.201
medium dense	0.253	0.251	0.246	0.240
dense	0.257	0.254	0.250	0.244
Second natural frequency (Hz)				
loose	1.041	1.024	0.984	0.932
medium dense	1.469	1.435	1.369	1.290
dense	1.541	1.503	1.430	1.346

In the present work, natural frequency of the monopile OWT is determined using the Lanczos algorithm. Figure 14 shows the reduction in the first natural frequency of the OWT, with increasing value of the scour parameter. Values of the first and second natural frequencies and their variation with scouring are given in Table 5. Scouring effectively increases the cantilever length of a monopile and reduces its stiffness and the natural frequency. For dense sand, the first natural frequency suffered a reduction of 5%, as the scour parameter increased from 0 to 1.5. This is in line with the work of [3], who reported a 5% reduction in the fundamental frequency of a 2 MW OWT for a scour depth increase to 1.3 times the diameter, in sand of high density. The corresponding reduction is higher in the case of loose sand (8%) and at s/D value of 1.5, the natural frequency is found to dip into the 1P region, where the OWT is vulnerable to resonance effects from environmental forces. This calls for periodic monitoring of natural frequency variations of the OWT. The second natural frequency undergoes a reduction of 13%, 12% and 10% for dense, medium dense and loose sands, respectively.

4.2. Ultimate Strength Analysis

Static pushover analyses are performed for an extreme sea-state represented by $H_s = 9.5$ m and $T_p = 12.8$ s. Wind loads acting at the top of the tower are not considered for the pushover analysis. Initially, time invariant loads acting on the OWT (gravity, in this case), are applied to their full value. During the second stage, the monopile is pushed to failure by gradually incrementing the lateral wave load [47].

The load - displacement curves obtained through pushover analysis, for varying soil properties are shown in Figure 15. Here, the base shear load is plotted against the pile top displacement. The secant modulus (defining the stiffness) of the p-y curves are directly dependent on the angle of internal friction (ϕ). This effect of structural stiffness is observed in the load - displacement curves. Irrespective of the nature of the soil, the removal of lateral support during scour and the associated reduction in the overall stiffness of the OWT structure results

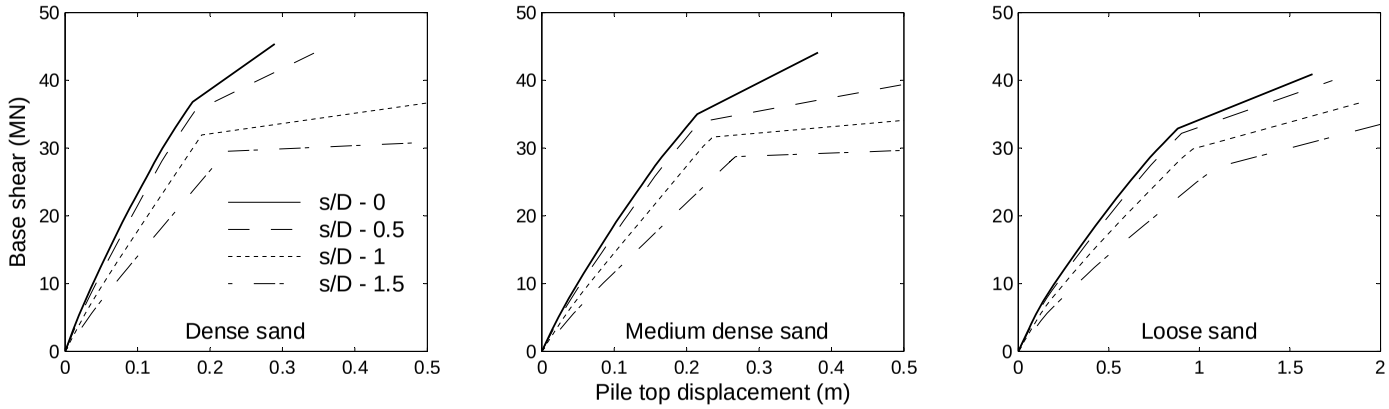

Figure 15: Pushover analysis of monopile OWT

in lower yield values.

Figure 16 shows the displacement profiles of the monopiles (below the mudline), at the initial yield of the OWT structure. Initial yield does not imply total failure of the structure, but refers to the introduction of an elasto-plastic hinge. Keeping the $s/D = 0$ profile as reference, it is observed that a scour parameter value of $s/D = 1.5$ brings about a percentage increase in pile top displacement at first yield, of 28%, 20% and 24% respectively, in dense, medium-dense and loose sands. The variation in the response mechanism of the monopiles with respect to soil stiffness is also worth noting. Piles in dense sand show plastic deformation in the upper soil layers and the toe-kick phenomenon (lateral displacement at the toe of the monopile) is absent. However, in the case of loose sand, the pile responds to heavy lateral loads by undergoing rigid body rotation, with prominent toe-kick.

4.3. Dynamic Analysis

The HHT-α algorithm [13] is used for dynamic analysis. Figures 17 and 18 show the variation in the maximum pile top rotation and displacement of the three soil profiles, under LC1 and LC2 respectively. These responses are ensemble average of maximum response obtained from 50 stochastic simulations. The analysis shows that these responses are highly nonlinear with skewness as 0.86 and kurtosis as 3.3. Even with a extreme sea state, LC2 generates a smaller response from the pile, than LC1, as the operation of the turbine is suspended at high wind speeds, resulting in reduced lateral aerodynamic loads at the hub. The pile top rotations were observed to fall within the stipulated serviceability criteria of 0.5°[5]. Also, the rate of increase of lateral response is observed to reduce with increase in density of the soil. For instance, in LC1s, the pile top displacement increases at 100% for dense sand, corresponding to an increase in the scour parameter from 0 to 1.5. For loose sand, this value drops to 50% as shown in Figure 17.

Figure 19 is indicative of the maximum lateral displacement of the pile nodes under dynamic loading, for load cases LC1 and LC2. Here, the absolute max-

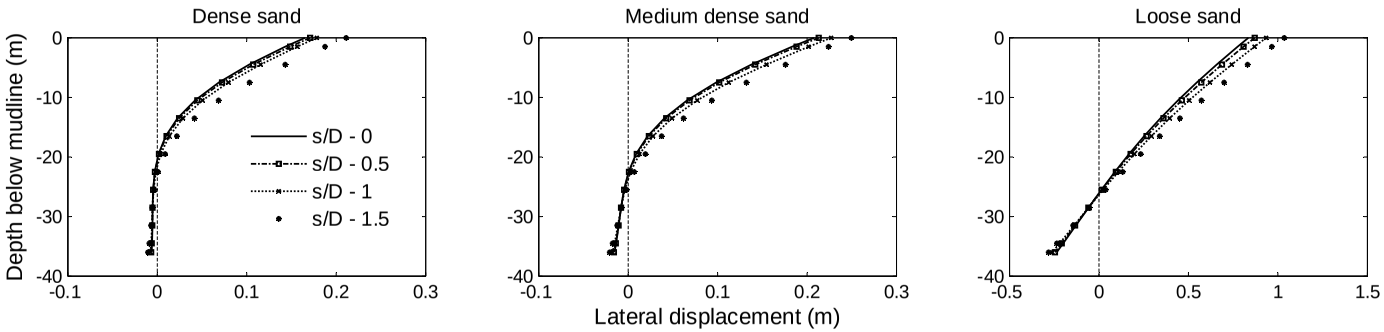

Figure 16: Pile profiles at first yield

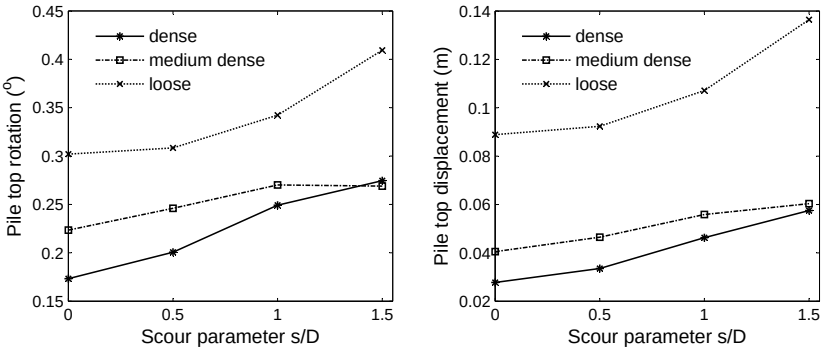

Figure 17: Pile top rotation and displacement response for operating load case (LC1)

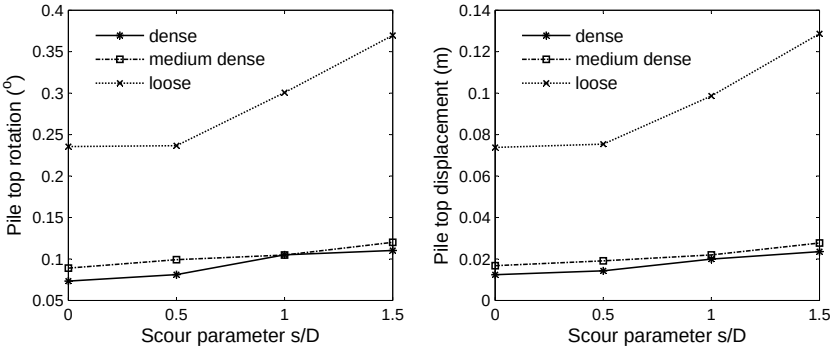

Figure 18: Pile top rotation and displacement response for operating load case (LC2)

imum value of nodal displacements, across the ensemble, are plotted against depth of the pile below the mudline. Due to the reduction in the aerodynamic load in LC2, the lateral displacement for piles in dense and medium dense sands show a significant reduction, by 50% along the depth of the pile. It is also noted that at lower levels of scour ($s/D = 0.5$), the displacement profile closely follows that of the no-scour condition. However, for loose sand, even the lower loads imposed by LC2 are able to elicit a significant lateral response.

The monopile seems to undergo rigid body rotation about a pivot point, leading to a toe-kick mechanism, as is evident from Figure 19, for loose sand. This rigid body rotation is not highly evident for the denser soil profiles. The pivot point is observed to move down along the length of the pile, with increase in soil density.

5. Conclusions

A numerical study on the influence of scour on monopile supported OWTs in sands of varying densities has been carried out, using FEM. Scour scenario was simulated by removing the necessary soil springs from the upper layers. Changes in natural frequency, yield and lateral response (by 50%) under aerodynamic and hydrodynamic loads are obtained for operational and extreme load cases. Results indicate that OWTs in loose sands are highly vulnerable to resonance effects of combined wind and wave loading, due to reduction in the natural frequency under scouring. Even as the serviceability criteria with respect to mudline rotation is satisfied, the monopile in loose sand exhibits rigid body rotation about a pivotal point. The study does not consider the effect of possible soil stiffness degradation due to cyclic loading. Also, the response of the OWT in the presence of back-fill material, aimed at mitigating the influence of scour, has to be investigated.

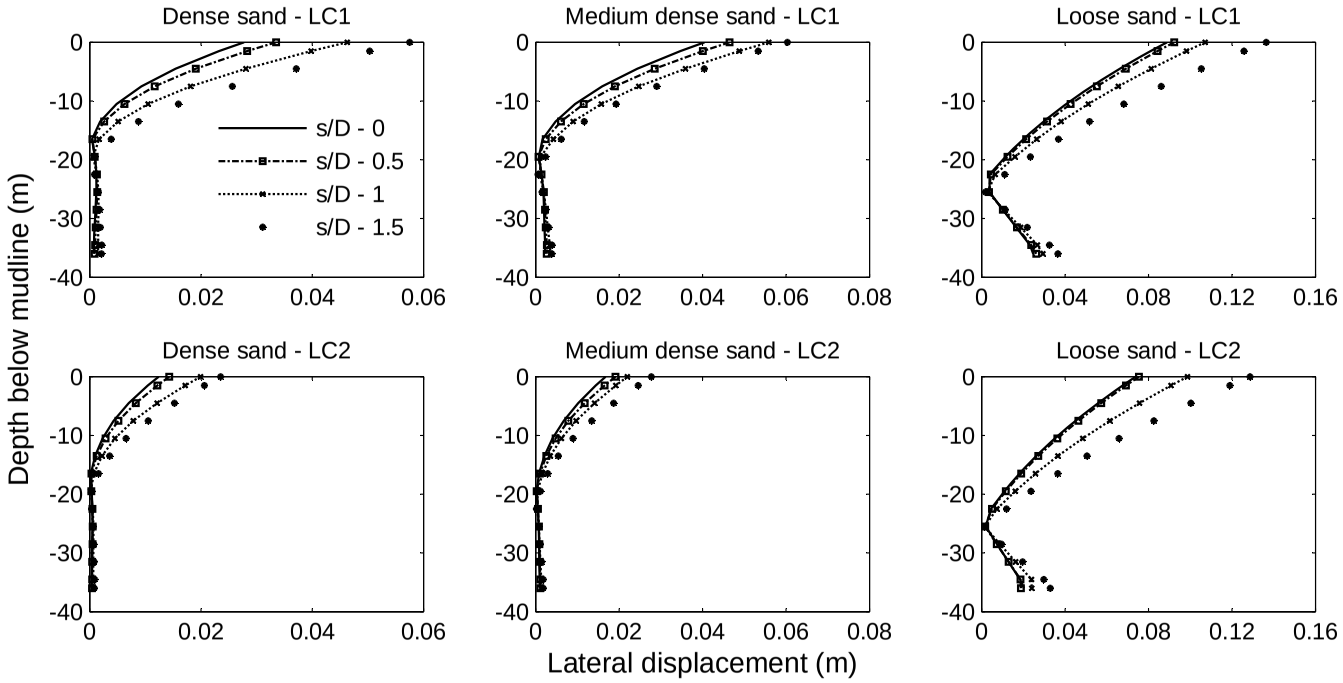

Figure 19: Maximum pile displacement configuration

6. Acknowledgments

The authors are grateful to Tøre Holmas of `www.usfos.no` for his guidance with USFOS. Jason Jonkman's help with FAST is also acknowledged.

[1] J. van der Tempel, M. B. Zaaijer, H. Subroto, The effects of scour on the design of offshore wind turbines, in: Proceedings of the 3rd International conference on marine renewable energy Marec, 2004, pp. 27–35.

[2] R. Whitehouse, Scour at marine structures: A manual for practical applications, Thomas Telford, 1998.

[3] S. P. H. Sørensen, L. B. Ibsen, Assessment of foundation design for offshore monopiles unprotected against scour, Ocean Engineering 63 (2013) 17–25.

[4] L. J. Prendergast, K. Gavin, P. Doherty, An investigation into the effect of scour on the natural frequency of an offshore wind turbine, Ocean Engineering 101 (2015) 1–11.

[5] M. Achmus, Y.-S. Kuo, K. Abdel-Rahman, Numerical investigation of scour effect on lateral resistance of windfarm monopiles, in: The Twentieth International Offshore and Polar Engineering Conference, International Society of Offshore and Polar Engineers, 2010.

[6] B. Skallerud, J. Amdahl, Nonlinear analysis of offshore structures, Research Studies Press Baldock, Hertfordshire,, England, 2002.

[7] N. Saha, Z. Gao, T. Moan, A. Naess, Short-term extreme response analysis of a jacket supporting an offshore wind turbine, Wind Energy 17 (1) (2014) 87–104.

[8] S. Voormeeren, P. Valk, B. Nortier, D.-P. Molenaar, D. Rixen, Accurate and efficient modeling of complex offshore wind turbine support structures using augmented superelements, Wind Energy 17 (7) (2014) 1035–1054.

[9] D. Zwick, M. Muskulus, The simulation error caused by input loading variability in offshore wind turbine structural analysis, Wind energy 18 (8) (2015) 1421–1432.

[10] DNV, OS-J101 Offshore Standard - design of offshore wind turbine structures (2011).

[11] API-RP2A-WSD, American Petroleum Institute-Recommended practice for planning, designing and constructing fixed offshore platforms- Working stress design (2007).

[12] J. M. Jonkman, S. Butterfield, W. Musial, G. Scott, Definition of a 5-MW reference wind turbine for offshore system development, Tech. Rep. NREL/TP-500-38060, National Renewable Energy Laboratory, Golden, Colorado (2009).

[13] T. H. Søreide, J. Amdahl, E. Eberg, T. Holmås, Ø. Hellan, USFOS-A computer program for progressive collapse analysis of steel offshore structures. Theory Manual, SINTEF (1993).

[14] K. Lesny, S. Paikowsky, A. Gurbuz, Scale effects in lateral load response of large diameter monopiles, Geotechnical Special Publication 158 (2007) 1–10.

[15] J. van der Tempel, D.-P. Molenaar, Wind turbine structural dynamics–a review of the principles for modern power generation, onshore and offshore, Wind engineering 26 (4) (2002) 211–222.

[16] J. F. Manwell, J. G. McGowan, A. L. Rogers, Wind energy explained: theory, design and application, John Wiley & Sons, 2010.

[17] DNV, Guidelines for design of wind turbines, Det Norske Veritas: Wind Energy Department, Ris National Laboratory, 2002.

[18] M. Karimirad, Offshore Energy Structures: For Wind Power, Wave Energy and Hybrid Marine Platforms, Springer, 2014.

[19] J. van der Tempel, Design of support structures for offshore wind turbines, Ph.D. thesis, TU Delft, Delft University of Technology (2006).

[20] B. J. Jonkman, Turbsim user's guide: Version 1.50 (2009).

[21] P. S. Veers, Three-dimensional wind simulation, Tech. rep., Sandia National Labs., Albuquerque, NM (USA) (1988).

[22] T. Burton, D. Sharpe, N. Jenkins, E. Bossanyi, Wind energy handbook, John Wiley & Sons, 2001.

[23] J. M. Jonkman, M. L. Buhl Jr, FAST – User's guide, Tech. Rep. NREL/EL-500-38230, National Renewable Energy Laboratory, Golden, Colorado (2005).

[24] M. O. L. Hansen, Aerodynamics of wind turbines, Routledge, 2015.

[25] M. O. L. Hansen, J. N. Sørensen, S. Voutsinas, N. Sørensen, H. A. Madsen, State of the art in wind turbine aerodynamics and aeroelasticity, Progress in aerospace sciences 42 (4) (2006) 285–330.

[26] F. D. Bianchi, H. De Battista, R. J. Mantz, Wind turbine control systems: principles, modelling and gain scheduling design, Springer Science & Business Media, 2006.

[27] K. Hasselmann, T. Barnett, E. Bouws, H. Carlson, D. Cartwright, K. Enke, J. Ewing, H. Gienapp, D. Hasselmann, P. Kruseman, Measurements of wind-wave growth and swell decay during the joint north sea wave project (JONSWAP), Tech. rep., Deutches Hydrographisches Institut (1973).

[28] K. S. Kumar, K. A. Kumar, Spectral characteristics of high shallow water waves, Ocean Engineering 35 (2008) 900–911.

[29] H. Benaroya, S. M. Han, M. Nagurka, Probability models in engineering and science, Vol. 193, CRC Press, 2005.

[30] S. O. Rice, Mathematical analysis of random noise, Bell System Technical Journal 23 (3) (1944) 282–332. doi:10.1002/j.1538-7305.1944.tb00874.x.

[31] S. O. Rice, Mathematical analysis of random noise, Bell System Technical Journal, The 24 (1) (1945) 46–156.

[32] S. Chakrabarti, Handbook of Offshore Engineering, Elsevier, 2005.

[33] M. A. El-Reedy, Offshore structures: design, construction and maintenance, Gulf Professional Publishing, 2012.

[34] A. H. Augustesen, K. Brødbæk, M. Møller, S. P. H. Sørensen, L. B. Ibsen, T. S. Pedersen, L. Andersen, Numerical modelling of large-diameter steel piles at horns rev, in: Proceedings of the Twelfth International Conference on Civil, Structural and Environmental Engineering Computing, Civil-Comp Press, 2009.

[35] W. Carswell, C. Fontana, S. R. Arwade, D. J. DeGroot, A. T. Myers, Comparison of cyclic py methods for offshore wind turbine monopiles subjected to extreme storm loading, in: ASME 2015 34th International Conference on Ocean, Offshore and Arctic Engineering, American Society of Mechanical Engineers, 2015, pp. V009T09A060–V009T09A060.

[36] L. C. Reese, W. F. Van Impe, Single piles and pile groups under lateral loading, CRC Press, 2010.

[37] G. Stewart, T. Moan, J. Amdahl, O. I. Eide, Nonlinear re-assessment of jacket structures under extreme storm cyclic loading: Part I - philosophy and acceptance criteria, in: Proceedings of the International Conference on Offshore Mechanics and Arctic Engineering, American Society of Mechanical Engineers, 1993, pp. 491–502.

[38] M. Mukhopadhyay, D. Choudhury, V. Phanikanth, G. Reddy, Pushover analysis of piles in stratified soil, in: Proc., 14th World Conf. on Earthquake

Engineering, Vol. 14, International Association for Earthquake Engineering (IAEE) Tokyo, 2008.

[39] SINTEF Group, Usfos getting started, Structural Engineering, Marintek.

[40] M. Seidel, F. Ostermann, A. Curvers, M. Kühn, D. Kaufer, C. Böker, Validation of offshore load simulations using measurement data from the DOWNVInD project, in: Proceedings of European Offshore Wind Conference, Stockholm, Sweden, 2009, pp. 14–16.

[41] Z. Gao, N. Saha, T. Moan, J. Amdahl, Dynamic analysis of offshore fixed wind turbines under wind and wave loads using alternative computer codes, in: Proceedings of the TORQUE 2010 conference, FORTH, Heraklion, Crete, Greece, 2010, pp. 1–9.

[42] W. Dong, Y. Xing, T. Moan, Time domain modeling and analysis of dynamic gear contact force in a wind turbine gearbox with respect to fatigue assessment, Energies 5 (11) (2012) 4350–4371.

[43] W. Carswell, S. R. Arwade, D. J. DeGroot, M. A. Lackner, Soil–structure reliability of offshore wind turbine monopile foundations, Wind Energy 18 (3) (2015) 483–498.

[44] K. Johannessen, T. S. Meling, S. Hayer, Joint distribution for wind and waves in the northern north sea, in: The Eleventh International Offshore and Polar Engineering Conference, International Society of Offshore and Polar Engineers, 2001.

[45] M. Karimirad, T. Moan, Wave-and wind-induced dynamic response of a spar-type offshore wind turbine, Journal of waterway, port, coastal, and ocean engineering 138 (1) (2011) 9–20.

[46] S. Bhattacharya, N. Nikitas, J. Garnsey, N. Alexander, J. Cox, D. Lombardi, D. M. Wood, D. F. Nash, Observed dynamic soil–structure interaction in scale testing of offshore wind turbine foundations, Soil Dynamics and Earthquake Engineering 54 (2013) 47–60.

[47] DNV, Ultiguide: Best Practice Guidelines for Use of Non-linear Analysis Methods in Documentation of Ultimate Limit States for Jacket Type Offshore Structures, Det Norske Veritas, 1999.